



**HAL**  
open science

# Different behaviours of the seismic velocity field at Soultz-sous-Forêts revealed by 4-D seismic tomography: case study of GPK3 and GPK2 injection tests

Marco Calò, Catherine Dorbath

► **To cite this version:**

Marco Calò, Catherine Dorbath. Different behaviours of the seismic velocity field at Soultz-sous-Forêts revealed by 4-D seismic tomography: case study of GPK3 and GPK2 injection tests. *Geophysical Journal International*, 2013, 194, pp.1119-1137. 10.1093/gji/ggt153 . insu-03620491

**HAL Id: insu-03620491**

**<https://insu.hal.science/insu-03620491>**

Submitted on 26 Mar 2022

**HAL** is a multi-disciplinary open access archive for the deposit and dissemination of scientific research documents, whether they are published or not. The documents may come from teaching and research institutions in France or abroad, or from public or private research centers.

L'archive ouverte pluridisciplinaire **HAL**, est destinée au dépôt et à la diffusion de documents scientifiques de niveau recherche, publiés ou non, émanant des établissements d'enseignement et de recherche français ou étrangers, des laboratoires publics ou privés.



Distributed under a Creative Commons Attribution 4.0 International License

# Different behaviours of the seismic velocity field at Soultz-sous-Forêts revealed by 4-D seismic tomography: case study of GPK3 and GPK2 injection tests

Marco Calò<sup>1</sup> and Catherine Dorbath<sup>1,2</sup>

<sup>1</sup>*Ecole et Observatoire des Sciences de la Terre, EOST, University of Strasbourg, Strasbourg Cedex, France. E-mail: calo@unistra.fr*

<sup>2</sup>*GET (IRD-UMR234)*

Accepted 2013 April 12. Received 2013 April 11; in original form 2012 October 19

## SUMMARY

The geothermal power plant of Soultz-sous-Forêts in Northeastern France consists of three boreholes (GPK2, GPK3, GPK4) reaching a depth of about 5 km. All the wells were stimulated through hydraulic injections. In this study, we present the results of a time-dependent (4-D) seismic tomography obtained with the *P*-wave arrival times of seismic events recorded in 2003 during the stimulation of the GPK3 well. The method combines double-difference tomography with the Weighted Average Model post-processing that corrects for parameter dependence effects. In light of additional processing of the continuous seismic records of 23 surface stations, some 4728 precisely located events were selected and separated into 13 subsets to examine periods defined with respect to the injection scheme. Particular attention is given to changes in injected flow rates, periods of stationary injection conditions, periods of dual stimulation with the GPK2 well and post-injection periods. Results confirm that significant structures crossing the well have controlled the evolution of the seismicity and have played a fundamental role in the distribution and amplitude of the seismic anomalies. Furthermore, the evolution of the seismic velocity field, together with the representation of the relocated seismicity, have been compared with the results of the 4-D tomography of the GPK2 well, which is located at only 600 m from the stimulated well.

**Key words:** Tomography; Seismic tomography; Rheology and friction of fault zones.

## 1 INTRODUCTION

At the EGS geothermal field of Soultz-sous-Forêts shown in Fig. 1(a) three wells (GPK2, GPK3, GPK4) reach a depth of about 5000 m. All the wells are not cased in the last 500 m. To connect the boreholes to the fracture network efficiently and to improve the overall permeability of the reservoir, GPK2 was stimulated in June/July 2000, GPK3 in May/June 2003 and GPK4 in September 2004 and again in February 2005. The reservoir development has now been completed and heat is exploited for conducting electricity.

During the different stimulations, several thousands events were detected and located (Cuenot *et al.* 2005, 2006, 2008; Charléty *et al.* 2006). Dorbath *et al.* (2009) observed different seismic responses during the stimulation tests of the three wells, particularly between GPK2 and GPK3, although the horizontal distance between the open sections is ~600 m (Fig. 1b). During the seismic sequence of GPK2, 718 earthquakes had a magnitude equal or greater than 1.0 and the largest a magnitude of 2.5. The *b*-value result of the Gutenberg–Richter law was higher than 1.2 (Cuenot *et al.* 2008; Dorbath *et al.* 2009), and the injectivity has been increased by a factor of 20 (Nami *et al.* 2007). These characteristics indicate that the stimulation reactivated a 3-D dense network of fractures. The

stimulation of GPK3 only induced approximately 250 events with a magnitude greater than 1.0 but with a greater number of large events (between 2 and 2.9). The hypocentres form clear structures identified as large faults, the *b*-value is about 0.9 and the large events ( $M > 2.0$ ) account for the greater part of the cumulative seismic moment (Charléty *et al.* 2006; Charléty *et al.* 2007; Dorbath *et al.* 2009). The injectivity of the well, which was already high before the stimulation, remained almost unchanged (Nami *et al.* 2007).

No borehole log data (Ultrasonic-Borehole-Image, Gamma ray, etc) are available for GPK2 below 3500 m depth, but the data collected in GPK3 give insights into the presence of large fractures crossing the well. In the open-hole section of GPK3, at about 4775 m, several fractures forming a fracture cluster striking 160°E on average and dipping between 40° and 70° are observed (Dezayes *et al.* 2004). During the drilling operation, most of the fluid was lost at this depth. Moreover, this zone corresponds to a loss of water of about 70 per cent during the 2003 stimulation and 60 per cent during a flow-log test 3 yr later with a 30 l s<sup>-1</sup> flow rate (Nami *et al.* 2008). A similar total loss was also observed close to the bottom of the same well, during the drilling operations, corresponding to a fracture zone identified at 4957 m. Another fracture zone with significant loss of water during flow-log measurements (greater than

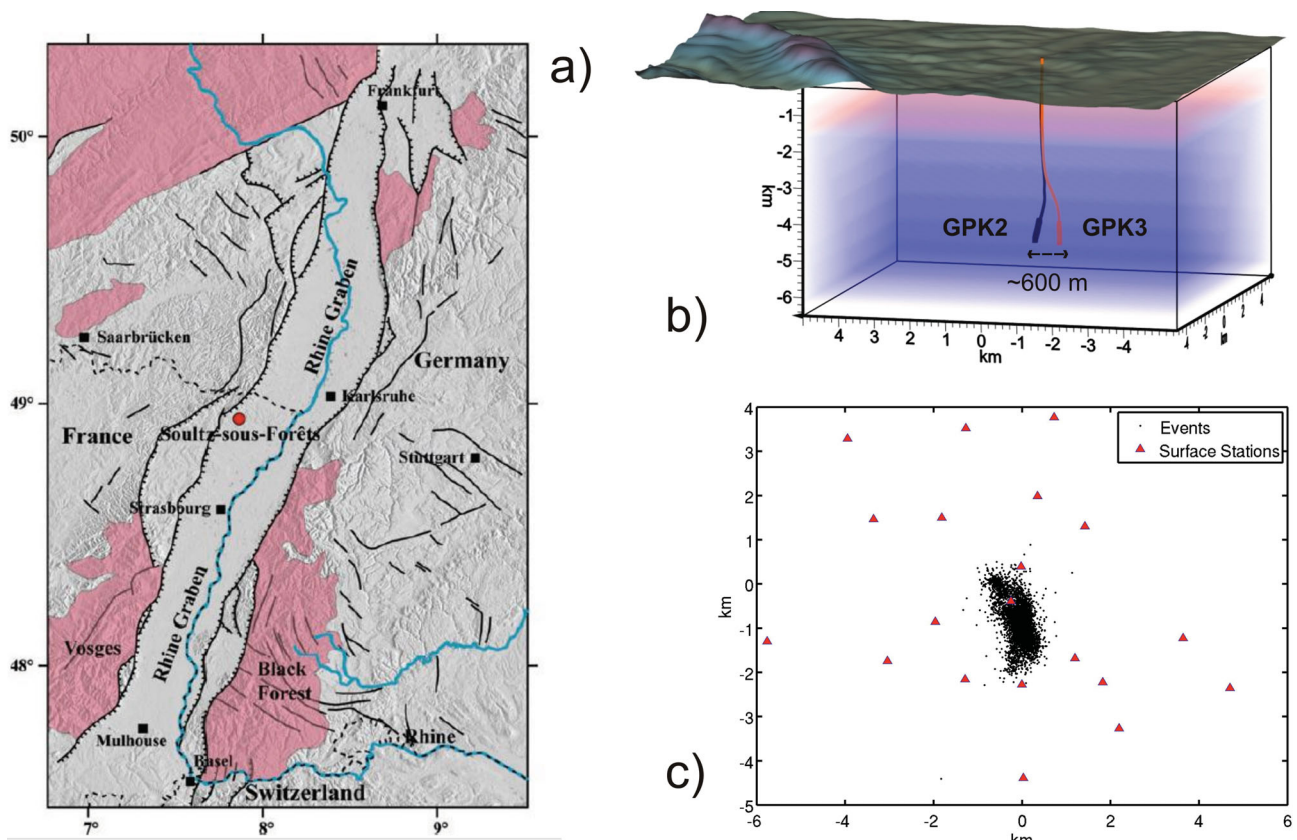


**Figure 1.** (a) Location of the Sultz-sous-Forêts EGS site in the Rhine Graben. Outcropping crystalline rocks are shown in pink; (b) Three-dimensional view of the GPK2 and GPK3 wells. The thick part of the boreholes corresponds to the open-hole sections of the wells; (c) Surface seismological stations (red triangles) installed during the 2003 stimulation test. Black dots are the epicentres of the events used for this study.

10 per cent) was found at 4905 m. The different seismic response of the reservoir to the GPK3 injection test compared with the GPK2 test was therefore interpreted as a consequence of such structures (Dorbath *et al.* 2009).

In this study, we present new results of a time-dependent (4-D) seismic tomography obtained by inverting  $P$ - and  $S$ -wave arrival times for seismic events recorded during the 2003 GPK3 stimulation. During this stimulation more than 7000 microearthquakes were recorded by the surface network (Charl y *et al.* 2006). Among them we have selected 4728 events detected by the seismic network which have magnitudes ranging from  $-0.9$  to  $2.9$ . As with Charl y *et al.* (2006), we performed the 4-D seismic tomography after dividing the main set into chronological subsets to describe temporal changes in the seismic velocity structure during the stimulation. This study differs from theirs in three main points: (i) the continuous seismic records were carefully reprocessed allowing a large increase of events selected for the tomography, (ii) the subsetting of the data has been performed by taking into account variations of injection parameters (i.e. injection flow rate, well-head pressure and down-hole pressure) and: (iii) the approach combines a double difference tomography method (tomoDD, Zhang & Thurber 2003) with an averaging process [Weighted Average Model (WAM), Cal  *et al.* 2009, 2011] that adjusts for parameter dependence effects. A comparison of these results with those of the 4-D tomography obtained for the GPK2 injection test (Cal  *et al.* 2011) offers insights into the different response of the reservoir for the two wells.

Finally, we discuss how the precise relocation of seismic events together with the temporal variations of the 3-D  $P$  velocity models facilitates the detection and description of some previously known

features of the stimulated reservoir and to individuate large new structures.

## 2 GPK3 STIMULATION

### 2.1 Injection parameters

To improve the connectivity and the permeability of the reservoir, GPK3 was stimulated through a high-pressure water injection that lasted more than ten days. During this stimulation test, over  $33\,000\text{ m}^3$  of fluids were injected in GPK3 and  $4300\text{ m}^3$  in GPK2. In contrast to the GPK2 stimulation, the GPK3 injection strategy was very complex (Fig. 2). We have divided the stimulation test into seven main phases according to the main variations of the injection parameters (Fig. 2). Phase 1 includes the first 60 hr of the stimulation where the injection flow rate was approximately constant at  $\sim 30\text{ l s}^{-1}$ . Phase 2 consists of the early period of the stimulation when the injected flow rate of GPK3 was increased to  $50\text{ l s}^{-1}$  for 72 hr. During this phase two ‘shots’ at 60 and  $93\text{ l s}^{-1}$  were tested for a period of a few hours. Phase 3 includes a dual stimulation and the injected flow rate was at  $50\text{ l s}^{-1}$  in GPK3 and  $25\text{ l s}^{-1}$  in GPK2, respectively. The injection in GPK2 lasted 32 hr while a pick at  $86\text{ l s}^{-1}$  was tested in GPK3 for a few hours. In Phase 4, the injection in GPK2 was stopped while the flow rate at GPK3 was decreased to about  $25\text{ l s}^{-1}$ . Phase 5 is a period of rest with no injections. Phase 6 includes a production period in GPK2 of 120 hr where water was pumped at about  $15\text{ l s}^{-1}$ . Phase 7 corresponds to the end of the stimulation test where all the wells were again at rest.

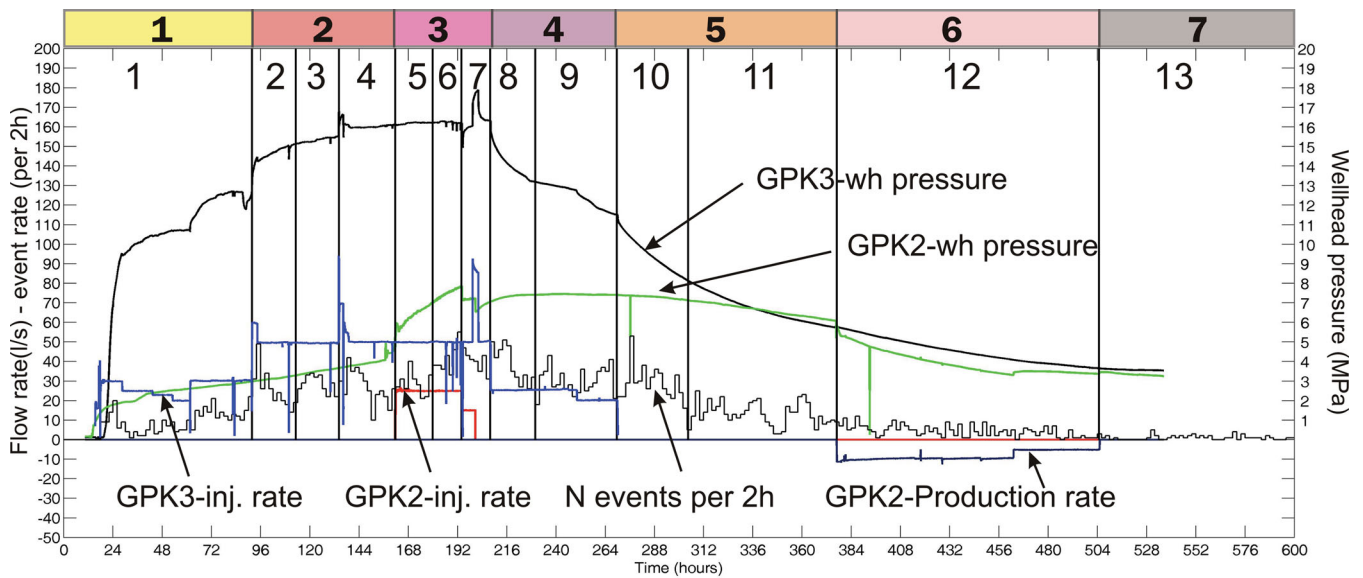


**Figure 2.** Injection rate (blue line for GPK3 and red line for GPK2) and overpressure (black line for GPK3 and green line for GPK2) measured at the well head. The event occurrence is also reported in the graph. The seven main phases are shown in the coloured rectangles and the subdivisions into 13 sets for the 4-D tomography are in black.

## 2.2 Data and method

As observed in the GPK2 injection test, intense microseismic activity was recorded during and after the GPK3 injection test. The seismic network installed by EOST, (University of Strasbourg) consisted of nine permanent surface stations supplemented by 14 temporary stations (Fig. 1c). They included 14 1C and nine 3C short period (1 Hz) seismological stations (Charl ty *et al.* 2006). The area covered by the network is centred on the EGS and is  $\sim 11 \times 9 \text{ km}^2$ .

The initial 1-D horizontally layered velocity model used for locating events was the same used to locate the events recorded during the GPK2 stimulation and derived from sonic logs and calibration shots performed in the GPK1 well (Beauce *et al.* 1991). To be consistent with previous studies, we chose GPK1 well-head (48.93537 N, 7.86535 E, altitude 153 m) as the geographical origin for this work.

Automatic processing of the data, based on an autoregressive algorithm (Leonard & Kennett 1999), detected and picked the arrival times (*P*- and *S*-phases) of about 7000 events. The method was set up and optimized for the Soultz region by Charl ty (2007). However after some further improvements and optimizations of the code routine, we reanalyzed the whole sequence of the continuous seismic records to augment the present data set. About 7500 triggers were detected and among them we selected 4728 events located using at least eight *P*- and three *S*-arrival times and located with a root mean square (rms) lower than 0.04 s. The events were located using on average 15 *P* and 5 *S* phases. After the location procedure the mean rms resulted in 0.021 s.

The reliability of the automatic procedure for detecting and picking the seismic phases was tested by comparing the picking of the *P*- and *S*-arrival times of the 250 largest events with the phases hand-picked for the same events (Dorbath *et al.* 2009). The difference between the automatic and manually picked phases (1000 *P* and 300 *S*) was on average 0.01 s and resulted in an absolute random displacement of the hypocentre positions of 30 m and 50 m in the horizontal and vertical directions, respectively. Because these differences are lower than the hypocentre error estimations we can

conclude that the automatic procedure does not significantly affect the reliability of the Soultz site data, at least for the larger events. Finally, we purposely included all the events collected by Charl ty *et al.* (2006) in our data set and the resultant hypocentre locations are very close. However, the new data set incorporates 2476 events that were excluded from the database of Charl ty *et al.* (2006). The main reason for this discrepancy is that we included events that occurred in a longer time period. The database collected by Charl ty *et al.* (2006) contains events recorded until the end of the stimulation test (2003 June 17) while we included the events that occurred up to 2003 July 12. Furthermore, during the overlapping period, several additional events were included in our data set because they were located with lower rms or detected by a larger number of stations. Finally the optimization of the automatic routine allowed for the detection of some new events not picked in the previous data set. Therefore this data set represents a more complete catalogue.

Hence we decided to apply the tomographic method to 13 unevenly populated sets to observe the seismic velocity variations during the time. The sets were set up according to the seven main phases described above (Table 1; Fig. 2). To study the reservoir response in detail, we considered the main variations of the flow rate (Sets 1, 2, 5, 7, 8, 10, 12 and 13) and we added steps when the injection parameters were maintained constant for long time periods (Sets 3, 4, 6, 9 and 11). Each set was used to calculate *P*- and *S*-wave velocity models using the same procedure as described by Cal  *et al.* (2011) to study seismic velocity variations during the GPK2 injection test. The approach combines a double-difference tomography method (Zhang & Thurber 2003) with an averaging process (WAM: Cal  2009; Cal  *et al.* 2011) that corrects for parameter dependence effects. Reliability tests on the tomograms calculated with the data of the GPK3 stimulation (described in Appendix A) show that the data and method are able to uncover weak differences  $> 1.5$  per cent in *P*-velocity structures with respect to the initial model. Although the *S*-velocity models were also calculated, the lack of experimental data does not allow a reliable assessment of these results. Consequently, in this work we will discuss only the *P*-wave velocity models.

**Table 1.** Time period, number of events, absolute data (*P* and *S*) and differential data (*P* and *S*) for the 13 sets.

Subset	Time period	N. events	Abs. <i>P</i> phases	Abs. <i>S</i> phases	Diff. <i>P</i> data	Diff. <i>S</i> data
1	06/30 hr 19:15 07/01 hr 03:40	351	3131	1162	32 839	9167
2	07/01 hr 03:41 07/01 hr 18:39	273	6443	1874	65 316	15 351
3	07/01 hr 18:39 07/02 hr 03:50	300	5807	2105	59 163	17 907
4	07/02 hr 03:50 07/02 hr 12:57	376	6807	1782	43 582	14 809
5	07/02 hr 12:58 07/02 hr 21:39	262	2246	674	23 429	6324
6	07/02 hr 21:46 07/03 hr 10:04	291	4382	900	44 049	6402
7	07/03 hr 10:04 07/03 hr 18:06	283	5836	2040	59 341	17 470
8	07/03 hr 18:07 07/04 hr 10:25	423	5745	2068	58 460	17 391
9	07/04 hr 10:32 07/04 hr 20:11	611	7192	2545	71 515	22 830
10	07/04 hr 20:12 07/05 hr 04:45	496	4493	1344	47 121	12 977
11	07/05 hr 04:47 07/05 hr 20:06	483	6701	2469	63 488	20 140
12	07/05 hr 20:07 07/06 hr 16:10	286	8659	3440	81 361	20 140
13	07/06 hr 16:10 07/07 hr 04:18	293	3213	1328	28 826	11 296

### 2.3 Temporal evolution of the *P*-wave velocity field during GPK3 stimulation

Thirteen WAMs have been computed from the thirteen sets reported in Table 1 to observe the temporal evolution of  $V_p$  field in the geothermal reservoir. The  $V_p$  value of the initial 1-D model is  $5.85 \text{ km s}^{-1}$  at 4.6 km depth. Thereafter, we discuss the seismic velocity anomalies with values greater or lower to  $\pm 0.08 \text{ km s}^{-1}$  from the initial 1-D model (i.e. 1.5 per cent of the initial model) and with standard deviation (WSTD)  $< 0.03 \text{ km s}^{-1}$  (see Appendix A).

The  $V_p$  models are shown in Fig. 3 (horizontal sections at 4.6 km depth) and Fig. 4 (vertical sections along the profile A–B in Fig. 3). In the figures, the red line represents the projection of GPK3 whereas the blue represents GPK2. The thick part of the GPK3 and GPK2 trajectories correspond to the open-hole section of the wells which are located within the 4.4 to 5 km depth interval. For all the sets, only the part of the model with Derivative Weight Sum (DWS; Toomey & Foulger 1989) greater than 10 is displayed. For each set we also report the projection of the events used to obtain the models. Black contours correspond to velocity iso-values equal to 5.77, 5.85 and  $5.94 \text{ km s}^{-1}$ .

Fig. 5 shows the final epicentre locations for the 13 sets whereas Fig. 6 shows the vertical projections along the NS direction. The size of the circle of each event is proportional to its magnitude. The mean rms is 0.014 s, and the mathematical uncertainty on the final locations is  $\sim 30 \text{ m}$  and  $\sim 50 \text{ m}$  for the epicentre and depth position, respectively.

#### Phase 1; Set 1

Set 1 shows the mean state of the reservoir during the first 3 days of the stimulation when the injection flow rate was almost always  $30 \text{ l}^{-1}$  (Fig. 2). At a depth of 4.6 km a low  $V_p$  area ( $5.55 < V_p <$

$5.77 \text{ km s}^{-1}$ ) is noted to the west of GPK3, about 200 m from the well. Its main elongation is N–S, although a NE prolongation of the  $V_p$  anomaly affects GPK3 (Fig. 3.1). The seismicity is centred on the stimulated well. The corresponding vertical section (Fig. 4.1) shows that the slight  $V_p$  anomaly affects only the GPK3 open-hole section whereas the seismicity covers a much larger area. Figs 5.1 and 6.1 display the relocated events of Set 1 as a compact cloud without any visible internal organization.

#### Phase 2; Sets 2–4

Set 2 includes events that occurred during the first 24 hr of Phase 2, when the injection rate was  $50 \text{ l}^{-1}$ . Fig. 3.2 shows the presence of a very weak low  $V_p$  anomaly ( $V_p \approx 5.7 \text{ km s}^{-1}$ ) located NW of the seismic cloud. The vertical section does not show velocity anomalies around the wells (Fig. 4.2). Seismicity of this set (Figs 5.2 and 6.2) is mainly centred on the well, although a small cluster is observed approximately 600 m from the stimulation region (black arrow in Fig. 5.2 at  $X = -100 \text{ m}$ ,  $Y = 0$ ).

In Set 3, when injection parameters are maintained constant, a low  $V_p$  anomaly is identified ( $5.67 < V_p < 5.77 \text{ km s}^{-1}$ ; Fig. 3.3) affecting the region around GPK3 and the western area where low velocities were already observed in Set 1. Its vertical extension is estimated to be 1 km (by taking as reference the iso-contour  $5.77 \text{ km s}^{-1}$ ; Fig. 4.3) whereas the horizontal extension (along the W–E direction) increases to 1.4 km. Here the seismic cloud is still centred on GPK3 and the seismicity located in the northern region has disappeared (Figs 5.3 and 6.3).

Set 4 includes the events that occurred until the end of this phase and the beginning of the dual stimulation. Injection parameters are mostly the same as the previous set and the resulting velocity model is similar, showing low  $V_p$  (Figs 3.4 and 4.4) and seismicity (Figs 5.4 and 6.4) centred around the stimulated well.

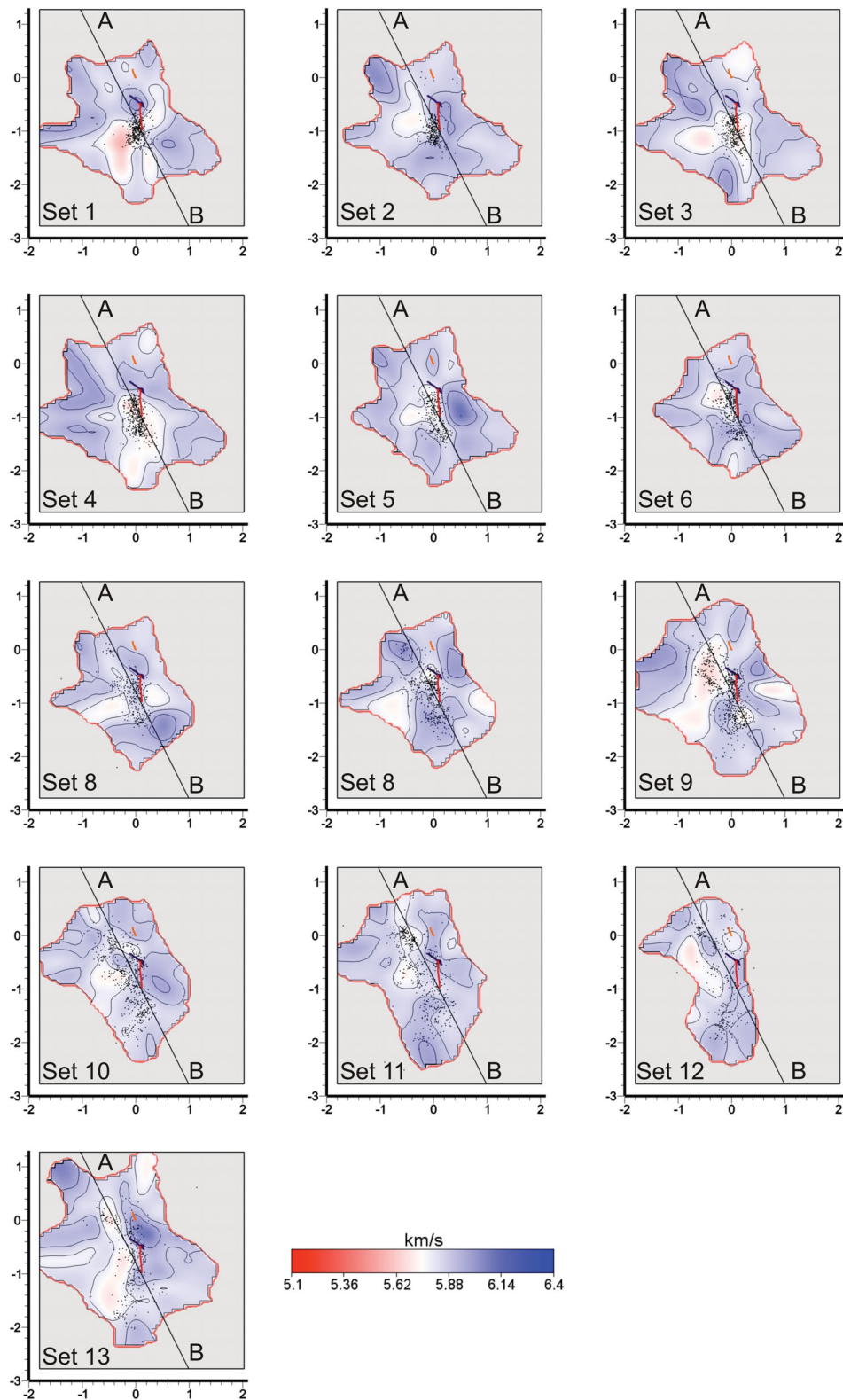


**Figure 3.** Evolution of the  $P$ -wave seismic velocity at 4.6 km depth during the 2003 stimulation test. Images are in chronological order from Set 1 to Set 13. The black dots are the projections of the events used to obtain the  $V_P$  models. Profiles A–B are the traces of the vertical sections reported in Fig. 4. Red and blue lines are the projections of GPK3 and GPK2, respectively.

### Phase 3; Sets 5–7

Set 5 includes events recorded during the initial 16 hours of the dual stimulation test. The injected flow rate was  $50 \text{ l s}^{-1}$  in GPK3 and  $25 \text{ l s}^{-1}$  in GPK2. Horizontal and vertical  $V_P$  sections

(Figs 3.5 and 4.5) report a low  $V_P$  region smaller than the previous set, and limited mostly to the region between the wells, whereas the seismicity remains located around GPK3 (Figs 5.5 and 6.5).

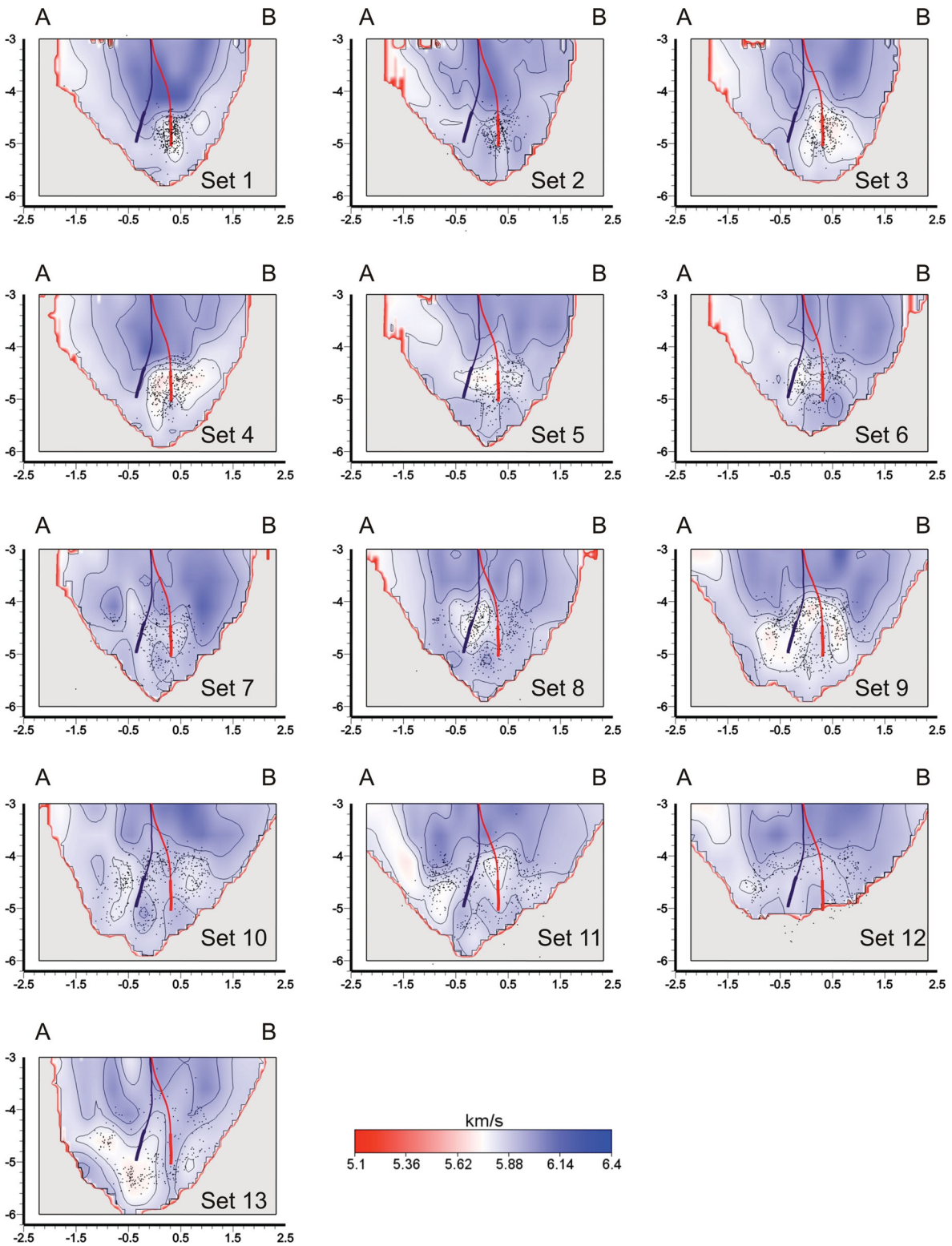


**Figure 4.** Vertical sections of the  $V_P$  models along traces A–B reported in Fig. 3. The black dots are the projections of the events used to obtain the  $V_P$  models. Red and blue lines are the projections of GPK3 and GPK2, respectively. The thick part of the borehole trajectories corresponds to the open-hole section of the wells.

In Set 6, the injection parameters remain constant. The area affected by the low  $V_P$  anomaly is more restricted and still located between the wells (Fig. 3.6). The vertical section shows that the weak low  $V_P$  anomaly is well centred on the open-hole section of GPK2 (Fig. 4.6). The seismicity is mainly located around GPK3

although a few events were recorded north of GPK2 (Figs 5.6 and 6.6) in the same area as observed in Set 2.

Set 7 contains the events recorded when the injection in GPK2 was stopped and a ‘shot’ at  $\sim 80 \text{ l s}^{-1}$  was tested in GPK3 for a few hours. Horizontal and vertical  $V_P$  sections are characterized by

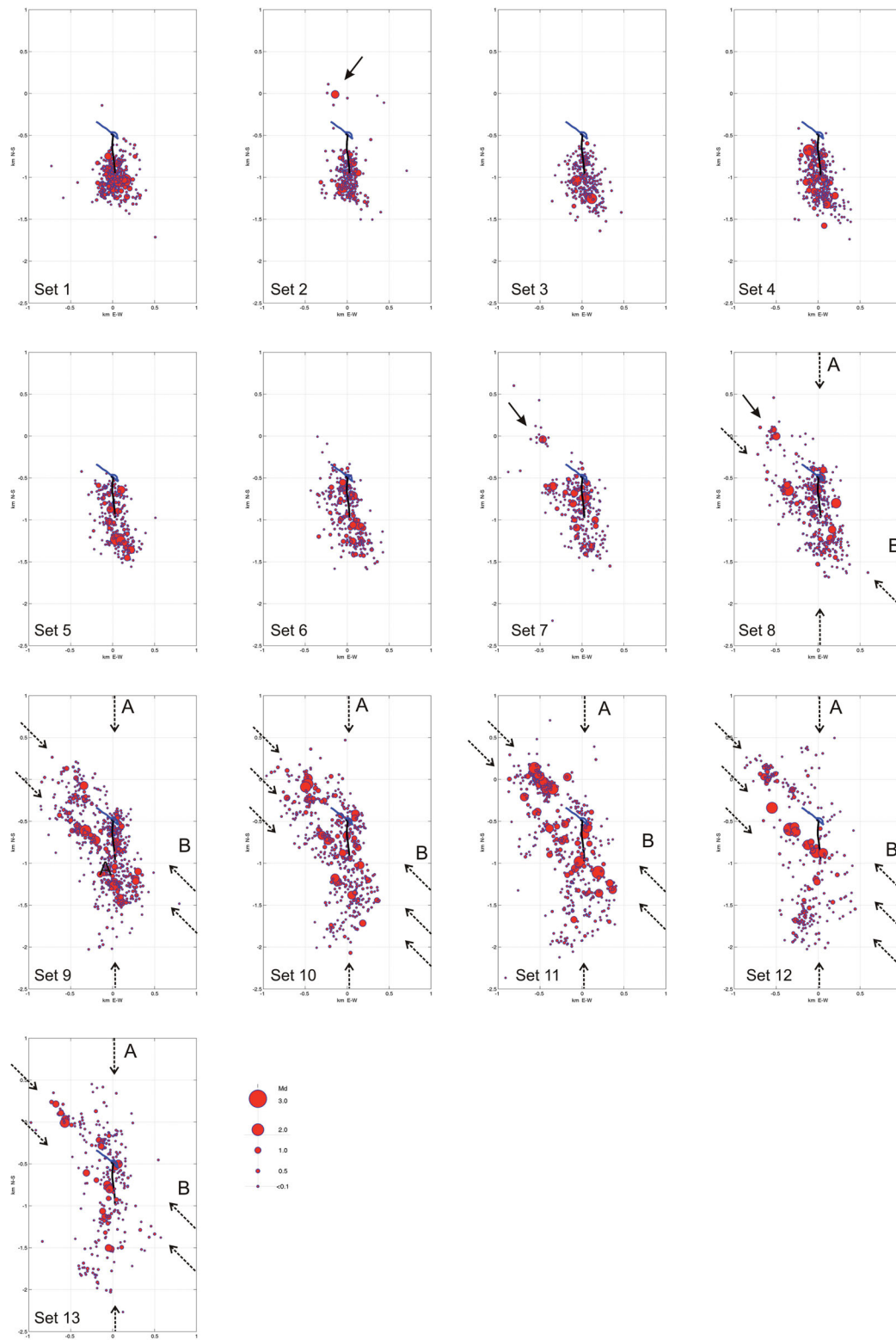


**Figure 5.** Evolution of the microseismic cloud. Each picture shows in chronological order the final epicentre positions after the computation of the local tomography. The radius of each circle is proportional to the magnitude and the projection of the injection well is indicated as a black line.

the quasi-total absence of velocity anomalies, showing only some patches in the eastern and western part of the larger seismic cloud (Figs 3.7 and 4.7). Seismicity is now organized into two main clouds instead, the larger located around the wells, the smaller located NW of GPK2 ( $X = -500$  m,  $Y = 0$  m; Figs 5.7 and 6.7).

#### Phase 4; Sets 8–9

Set 8 shows the mean state of the reservoir during the first 24 hr of Phase 4, when the injection rate in GPK3 was at  $25 \text{ l s}^{-1}$  (Fig. 2). A small low  $V_p$  anomaly ( $V_p \approx 5.77 \text{ km s}^{-1}$ ) is observed around GPK2 and a larger one at the western border of the resolved area. These

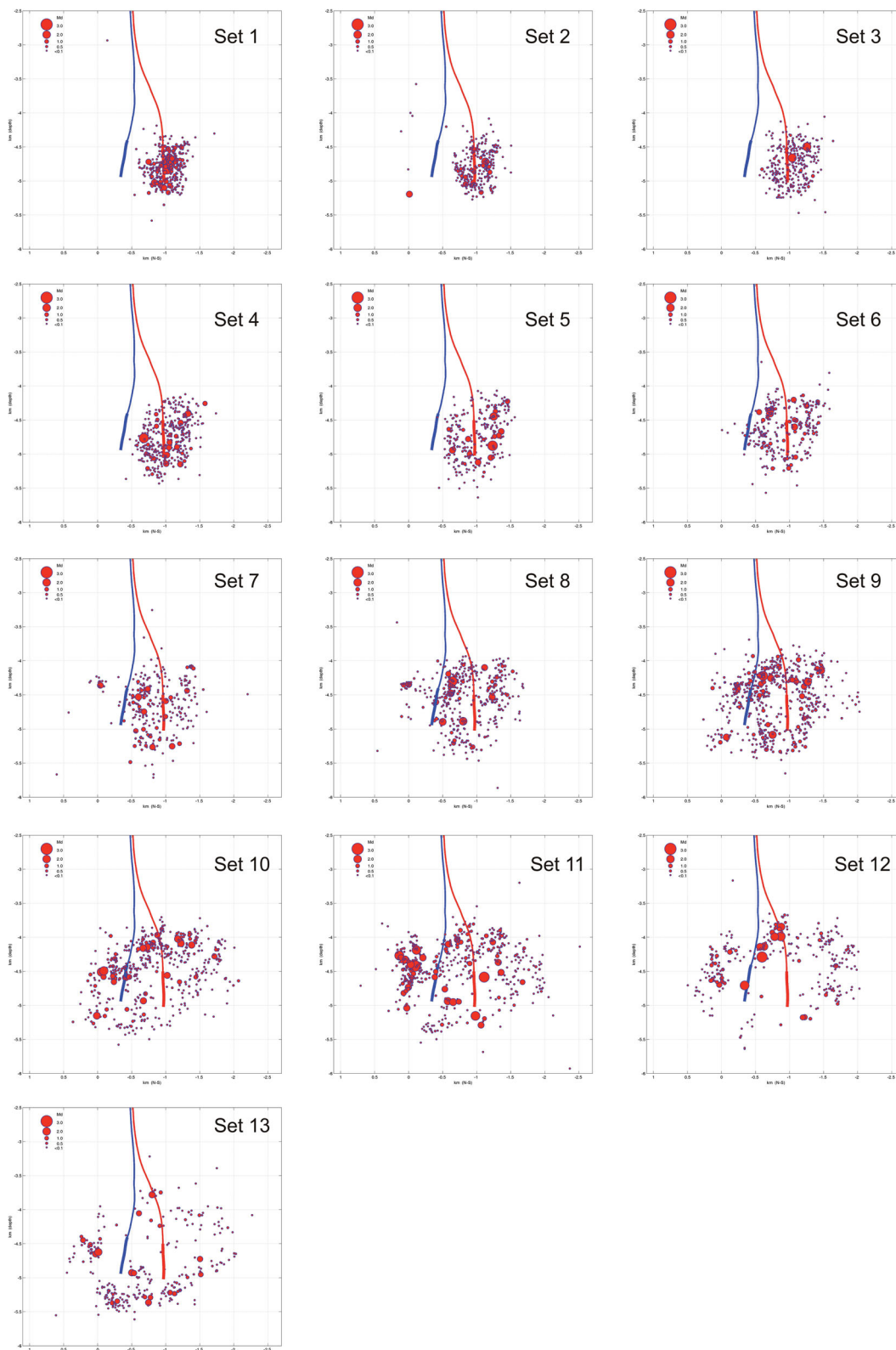


**Figure 6.** North–south vertical projections of the evolution of the microseismic cloud.

anomalies are not spatially correlated with the seismic clouds (Fig. 3.8). The vertical section of Fig. 4.8 shows the almost complete absence of  $V_p$  anomalies at depth of the stimulation, whereas a slight anomaly ( $V_p \approx 5.77 \text{ km s}^{-1}$ ) is observed around GPK2.

The two seismic clouds are apparent once again (Fig. 6.8) and the main cluster exhibits an internal organization of the seismicity, outlining at least two major active structures. The preferential directions are N–S (letter A in Fig. 5.8) and NW–SE (letter B in

Fig. 5.8). This internal pattern was discernible though hardly visible in the previous sets.

Set 9 shows a low  $V_p$  anomaly ( $5.6 < V_p < 5.77 \text{ km s}^{-1}$ ) that develops NW of the seismic cloud (Fig. 3.9). In the vertical section (Fig. 4.9) the low  $V_p$  body depicts a particular shape from 4 to 5.4 km depth bordering the area around the open-hole part of GPK3. The two seismic clouds (Fig. 5.9) observed in the previous sets now nearly merge and involve an extensive area of  $2.5 \times 1.5 \text{ km}^2$ . Seismicity shows that the main direction of the major seismic cloud (A) is cut by two internal seismic structures with direction B (Fig. 5.9). Most of the largest events that occurred in this period are located in the shallow reservoir, between 4 and 4.5 km of depth (Fig. 6.9).

#### Phase 5; Sets 10–11

Sets 10 and 11 include events recorded during the four days following the shut in. Both models show very slightly low  $V_p$  anomalies ( $5.73 < V_p < 5.77 \text{ km s}^{-1}$ ) at depth of the stimulation (Figs 3.10 and 3.11). Vertical sections highlight the absence of important anomalies, showing only small regions marked by low  $V_p$  north of GPK2 (Figs 4.10 and 4.11). The region affected by the seismicity is much larger than the low  $V_p$  anomalies mentioned above. However, the relocated seismicity (Figs 5.10, 5.11 and 6.10, 6.11) still depicts the internal seismic structures observed in the previous sets. In these sets at least three large seismic structures striking in the B direction are identified. In Set 11, the northern seismic cluster is characterized by intense activity and contains the largest magnitude event ( $M_d = 2.9$ ) recorded during the whole injection test.

#### Phase 6; Set 12

Set 12 includes events that occurred when water was pumped at  $15 \text{ l s}^{-1}$  from GPK2. At 4.6 km, depth only a slightly low  $V_p$  anomaly ( $5.7 < V_p < 5.77 \text{ km s}^{-1}$ ) is present west of the wells (Fig. 3.12). The vertical section shows a total absence of anomalies (Fig. 4.12) and the seismicity occurs in the shallow part of the reservoir, between 4 and 4.6 km of depth. The horizontal projection of the seismicity displays at least three main structures along B, and one mainly oriented N–S (A, Fig. 5.12). The vertical projection of the hypocentres (Fig. 6.12) shows that most of the major events are located in the shallow part of the cloud at 3.6–4.3 km of depth.

#### Phase 7; Set 13

The last set includes the events recorded in the month following the stimulation test. A low  $V_p$  anomaly ( $5.7 < V_p < 5.77 \text{ km s}^{-1}$ ) is observed at depth of the stimulation and mainly orientated N–S and NW–SE (Fig. 3.13). The vertical section shows a low  $V_p$  anomaly near GPK2 that develops northwards (Fig. 4.13). Notably, no low  $V_p$  residual anomalies are observed near GPK3, and the relocated seismicity (Fig. 5.13) depicts the same patterns observed in the previous sets.

### 3 COMPARISON OF THE GPK3 AND GPK2 STIMULATIONS

#### 3.1 Summary of the tomography results of the GPK2 stimulation test

The time-lapse tomography of the GPK2 injection (Calò *et al.* 2011) has allowed us to identify temporal changes of the  $V_p$  velocity field during and after the stimulation test carried out in 2000. Fig. 7 indicates four representative sets of the 4-D tomography together with the relocated seismicity (Sets 2, 3, 4 and 14). Fig. 8(a) depicts the

injection parameters recorded during the test along with the subset separation. In Appendix B, the 14 velocity models and the relocated seismicity obtained for the whole injection test are reported.

The main results of this 4-D tomography can be summarized by three main points (Calò *et al.* 2011):

(1) All the sets except Set 3 and Set 6 present highly similar features: a low-velocity anomaly mainly located around the zone where microseismic activity develops, but larger than the seismic cloud (Appendix B). Immediately after initiating the injection, the velocity anomaly is circular in shape as shown in Appendix B (Set 1). It elongates in the N145–N150°E direction during Set 2 (Fig. 7), and this direction remains constant over the whole injection period.

(2) Sets 3 and 6 represent the reservoir during the initial hours after an injection rate increase by  $10 \text{ l s}^{-1}$ , and show a return of the seismic velocity field to its initial value within the injection region (Fig. 7 and Appendix B).

(3) Relocated seismicity shows a seismic cloud centred on GPK2 striking in the NNW–SSE direction for the entire injection period, with only the post-injection seismicity (Fig. 7, Set 14) revealing some large internal structures.

The low  $V_p$  anomalies were interpreted as because of the presence of large rock mass volumes affected by changes in effective stresses, whereas the  $P$ -wave velocity variations within the reservoir (and consequently the related variations of effective stress) are not associated with simple water diffusion from the injection well, but rather reflect the occurrence of large-scale aseismic motions in the reservoir.

#### 3.2 Comparison of the two stimulations

The different behaviours of the GPK2 (2000) and GPK3 (2003) stimulations have been noted and discussed by several authors (Dezayes *et al.* 2005; Nami *et al.* 2008; Dorbath *et al.* 2009). A direct comparison of GPK2 and GPK3 velocity model results is difficult to obtain for the following reasons: (i) in 2000 the water was injected at 5 km depth in an ‘uncontaminated’ rock volume whereas in 2003 a large part of the reservoir was already enhanced because of the previous stimulation of GPK2 at the same depth; (ii) the adopted ‘injection strategy’ was different.

However some trends relative to the two injections are quite similar, allowing a comparative analysis of the two  $V_p$  seismic evolutions. The main differences have been summarized in four main points, concerning the size, shape and intensity of the low seismic velocity anomalies and the induced seismicity location pattern.

(1) During the GPK2 injection test, a low  $V_p$  anomaly is always present near the well and assumes a well-defined shape. Seismicity is generally located in a smaller area inside the low  $V_p$  region. Conversely, during the GPK3 injection the low  $V_p$  anomaly changes shape continuously and the region affected by the seismicity often varies with respect to the position of the seismic velocity anomalies.

(2) The lowest values of velocity anomalies in the GPK2 tomography were  $5.2$ – $5.3 \text{ km s}^{-1}$  (i.e. the 8–10 per cent of the velocity values of the reservoir at rest) whereas during most of the GPK3 stimulation the lowest values did not exceed  $5.6$ – $5.7 \text{ km s}^{-1}$  (i.e. 3–5 per cent).

(3) The post-injection period of the GPK2 test (Fig. 7, Set 14) is characterized by a low  $V_p$  anomaly affecting a large area while for the corresponding period of the GPK3 injection seismic tomography (Figs 3 and 4, Set 13) shows a slightly low  $V_p$  body oriented NS

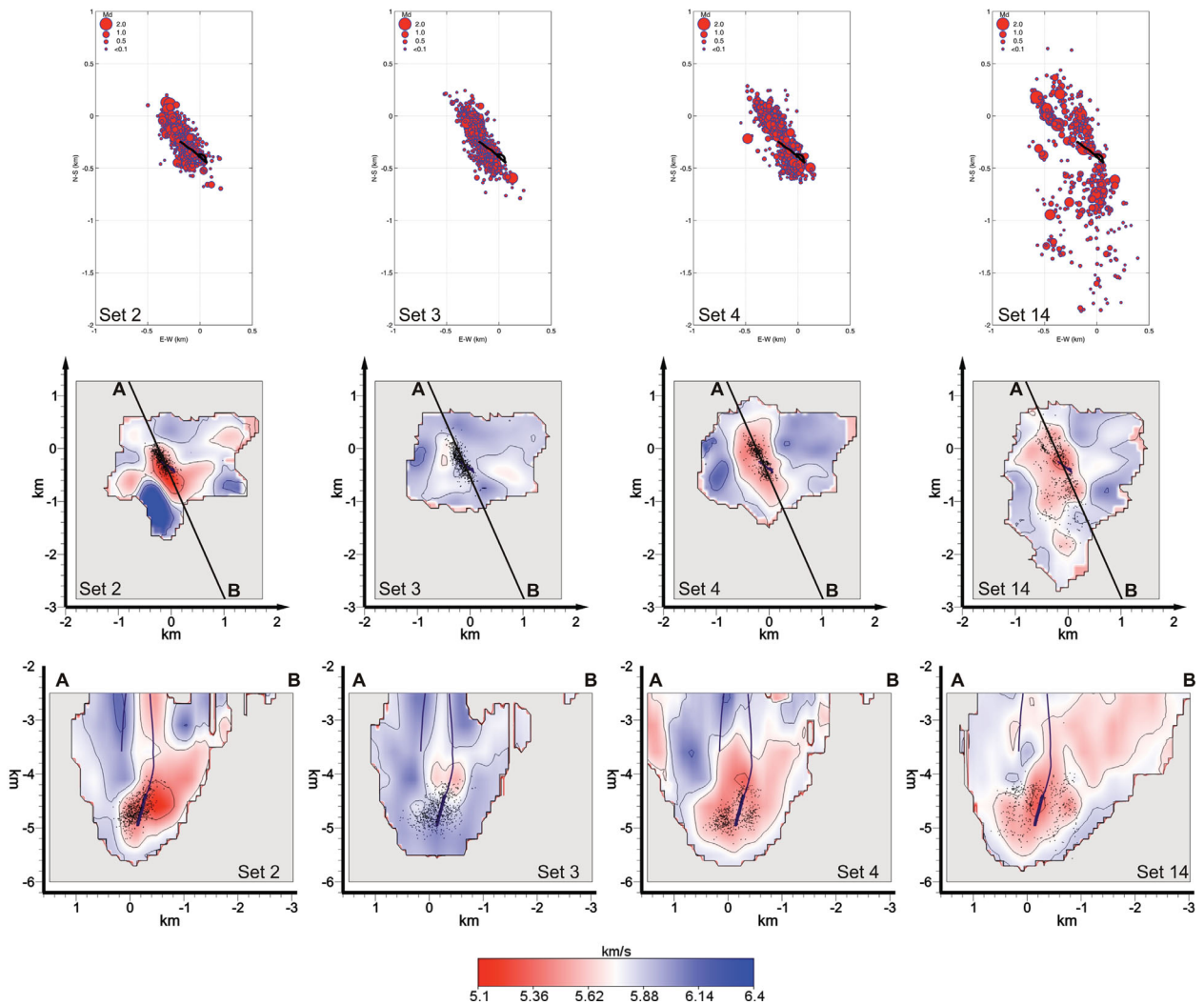


**Figure 7.** Evolution of the microseismic cloud (top) and of the  $P$ -wave seismic velocity models (bottom) of the GPK2 stimulation test performed in 2000 (after Calò *et al.* 2011). Set numeration is reported in Fig. 8a.

in the central and southern region, and oriented NNW–SSE in the northern region.

(4) The seismic clouds observed in GPK2 (Appendix B) are always dense and without internal structures until the shut in, and only the post-injection seismicity reveals some large structures (Fig. 7). On the contrary, seismicity recorded in 2003 underlines several seismic structures (directions A and B in Fig. 5) that are also evident during the stimulation period. Furthermore a small cloud clearly far from the stimulation region appears in a northern sector of GPK2 in the early phases of the injection.

Yet some interesting similarities are also revealed during the two stimulation tests, particularly concerning the temporal evolution of the velocity models. These similarities can be summarized in two main points.

(1) Tomograms of Sets 2, 3 and 4 relative to the GPK2 injection (Fig. 7) describe the seismic velocity variations when the injection rate was increased from 30 to 40  $\text{l s}^{-1}$ . In Set 3, the very low anomaly observed in Set 2 disappears, only to reappear in Set 4. Set 3 shows the presence of a weak  $V_P$  anomaly ( $V_P \approx 5.7 \text{ km s}^{-1}$ ) located west of the stimulated well. In the tomography of GPK3, Sets 1, 2 and 3 (Figs 3 and 4) are comparable to a similar step, even though the

injection flow rate was increased from 30 to 50  $\text{l s}^{-1}$ . These three sets show that GPK3 behaved similarly to GPK2, even if the low  $V_P$  anomalies observed are much weaker.

(2) The post injection seismicity of both injection tests (Set 14 for GPK2 and Set 13 for GPK3) reveal similar patterns showing that the seismicity recorded in 2000 after the shut in (Fig. 7, Set 14) is located along the same active structures depicted by the seismicity recorded during the 2003 stimulation (Fig. 5, Set 13).

Finally, we also compared the relation between the occurrence of the largest earthquakes and the injection parameters of the two stimulations. Fig. 8 shows the well-head pressure and injected flow rate of the GPK2 and GPK3 injection tests, together with the occurrence of the earthquakes of magnitude greater than 1.7. In 2000, 89 events occurred during the stimulation but only 17 in the 5 d after the shut in (Fig. 8a). The largest events occurred during static conditions of the injection parameters (e.g. Sets 10 and 11). Conversely, in 2003 most of the events (31 of 56) occurred in the periods of rest or during the GPK2 production period (Fig. 8b). The largest events occurred in Sets 8, 11 and 12 corresponding to periods marked by sudden reductions of the injected flow rate or during production periods. Furthermore, no correlation between the largest events and the increasing of flow rates was observed in either stimulation test.

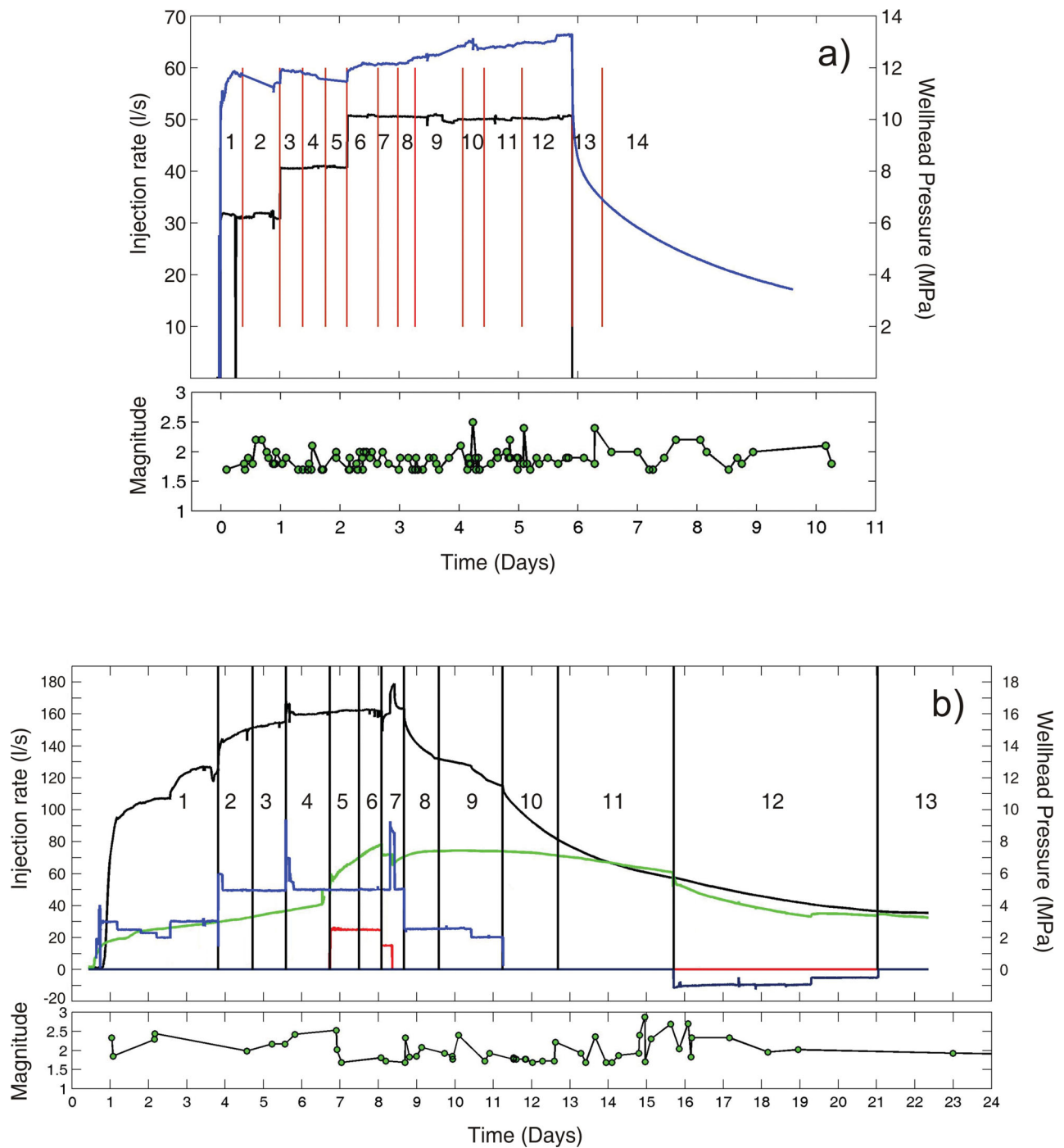


**Figure 8.** Injection parameters of the GPK2 (a) and GPK3 (b) injection tests. Also reported in the graphs are the temporal subsetting for the construction of the 4-D tomographies and the occurrence of the events with magnitude larger than 1.7 (green circles).

#### 4 DISCUSSION

The 4-D seismic tomography of the GPK3 stimulation occurred in 2003 at Soultz-sous-Forêts, and comparing it with the 4-D tomography of the GPK2 stimulation test (Calò *et al.* 2011) highlights strong differences in the behaviour of the geothermal reservoir during the two injections.

Synthetic tests and spatial analysis of the WSTD (Appendix A) assessed the reliability of the tomograms, which reveals the possibility of imaging weak structures (1.5 per cent of the initial model)

in the border regions as well. Julian & Foulger (2010) showed the risk of misinterpreting the artefacts related to the different ray path coverage of data collected in different epochs as temporal changes in the seismic velocity models. In the case of the Soultz injections this problem is negligible because the seismicity occurs in a restricted area with respect to that covered by the seismic network; consequently the ray path coverage rarely varies during stimulation periods. This was already determined by synthetic tests presented by Calò *et al.* (2011). Another cause that could affect time domain tomography is the presence of high levels of random errors

in the data. This problem is greatly reduced by the application of WAM post-processing. Calò *et al.* (2009, 2012), using regional earthquakes, have demonstrated that the WAM method reduces the effect of random errors, along with those related to the optimization of the input parameter that needs to impose the set up of a seismic tomography at the outset. Therefore, the temporal variations of the seismic velocities imaged at Soultz can be related to the variations of the physical properties of the geothermal reservoir during the injection tests.

In the GPK2 stimulation, the low  $V_p$  anomalies were related to the increasing of effective stresses in the regions around the well. Schoenball *et al.* (2012), using a data set of 715 events ( $M_d > 1$ ) recorded during the stimulation of GPK2, suggested that the Coulomb failure stress (DCFS) by dislocation is only a minor contribution to the whole stress perturbation induced by stimulation, whereas it can be quite effective for rupture propagation along single large fault zones. Hence, the stress drop produced by the seismicity alone does not justify the variation of the seismic velocities. This consideration supports the occurrence of some mechanism (such as the aseismic slips) accommodating the transient stress perturbation.

During the GPK3 stimulation, such low velocities were not observed. Dezayes *et al.* (2003, 2004) identified a  $\sim 10$  m structure crossing GPK3 at depth of the stimulation. Flow-log tests determined that about 70 per cent of the water injected in GPK3 is absorbed by this fracture (Dezayes *et al.* 2004). As a consequence, the transmissivity of GPK3 after the stimulation test increased only by a factor of 1.6 (Nami *et al.* 2008; Schindler *et al.* 2008). Conversely, the increasing of transmissivity after the GPK2 injection test was by a factor 19 (Nami *et al.* 2008). Several seismic structures, some of them crossing the GPK3 well, are clearly revealed by the relocated seismicity (Fig. 5). It is therefore possible that the fluids moved quickly throughout these preferential paths, affecting regions more than 900 m from the injection point, while still in the early phases of the stimulation. This leaking of water resulted in low effective stress changes in the region close to the GPK3 open-hole section. The presence of small seismic clouds and low  $V_p$  in regions far from the stimulated well (Sets 1, 6 and 7) support this interpretation. Thus the absence of low  $V_p$  anomalies during the GPK3 stimulation is explained by most of the injected water rapidly moving far from the injection region, avoiding an increase in the effective stress near the well.

In the first phases of the stimulation the seismic cloud is dense and is mainly concentrated around the GPK3 open-hole section until Set 4 (Fig. 6). After this phase (Set 5, i.e. when dual stimulation started) the seismic pattern changed. The region close to GPK3 became progressively aseismic and the seismicity spread out and moved towards shallower depths (Fig. 6). This suggests that the opening of the preferential fluid paths occurs during well-defined time periods. Regions close to the well end up aseismic and they should be interpreted as regions where the pore pressure does not increase because the fracture system is sufficiently developed and/or oriented in favourable directions with respect the regional stress field. This behaviour is also known as the Kaiser Effect.

However, the main paths of water drainage should not only be the seismic structures imaged by the seismicity. In the GPK2 tomography we observed that large aseismic slips should occur during particular phases of the injection test, and we cannot exclude the possibility that similar processes also affected the reservoir during the GPK3 stimulation. Indeed in GPK3 a scenario similar to that described in the GPK2 stimulation was observed when the injection flow rate was increased. In both stimulations (2000 and 2003), the low  $V_p$  anomalies disappear only to reappear after a period of time,

even if they differ in intensity and shape. This observation suggests that at such times a similar mechanism triggers some physical processes affecting the seismic velocity field. However, if in GPK2 the fading of  $V_p$  anomalies has been interpreted through the occurrence of large aseismic slips accommodating the increase in effective stress, the same cannot be assumed for GPK3 because the velocity variations observed are too weak.

The seismic velocity models were calculated using the data recorded during Phase 3 (Fig. 2), which allows observations of the interaction between the GPK3 and GPK2 wells during the dual injection. The sequence of Sets 4–6 (Figs 3 and 4) reports a gradual reduction of the slightly low  $V_p$  region and its migration from GPK3 to GPK2. The tomogram of Set 7 shows the total absence of  $V_p$  anomalies while they appear again in Set 8 in a region near GPK2. In Set 9, the low  $V_p$  grows and migrates towards GPK3 surrounding the open-hole section of the well (Fig. 4.9). The weakness of very low  $V_p$  values around GPK2 suggests that the presence of the dense fracture network is sufficiently developed (already present in 2000), allowing a rapid diffusion of the fluids at the flow rate tested in 2003. Despite the large amount of water injected at that time (a total of  $75 \text{ l s}^{-1}$ ), the dense fracture network avoided the accumulation of effective stresses near the wells, which resulted in a complete absence of seismic velocity anomalies. This condition is generally expected in the periods of rest or when the stress field is transiently reported to the initial conditions, as it was observed in 2000 when the flow rate was suddenly increased.

Noteworthy is the pattern depicted by the seismicity recorded in 2000 and 2003. The post-injection events allowed for observation of well-defined structures which affect the whole geothermal reservoir and that are associated with the largest events that occurred in the northern part of the Soultz reservoir.

Finally, the relation between the occurrence of the largest events and the injection parameters (Fig. 8) shows that a network of pre-existing fractures plays a fundamental role in the repartition of the transient stress perturbations during massive hydraulic stimulations. In 2000, this network was not well developed and the largest events occurred during the injection, where the stress perturbation was expected to be the highest. In 2003, the largest events occurred in periods marked by sudden reductions of the injected flow rate or during production periods when a decreasing of the pore pressure was expected in the reservoir. Furthermore, for both stimulations the occurrence of the largest events seems independent of the sudden increasing of the injected flow rate.

## 5 CONCLUSION

We propose that a large network of faults, some of them crossing GPK3, affected the repartition of the effective stresses around the well during the stimulation test. The presence of these structures represented the main paths of the injected water, and avoided the accumulation of effective stresses in the reservoir close to the GPK3 well. This resulted in a lack of large low  $V_p$  anomalies during the stimulation. The injected water affected a large region activating structures far from the origin point of the stimulation. The presence of faults, some of them crossing GPK3, is revealed by the relocated seismicity and the weak variations of the  $V_p$  models are consistent with small stress perturbations of the reservoir near the injection well.

However a similar evolution occurred during the GPK3 and GPK2 stimulations when injected flow rates were suddenly varied. This suggests the occurrence of a similar mechanism for

accommodating the variation of the effective stress close to the wells when rapid variations of flow rate are imposed. Because this mechanism, while affecting the seismic velocities, cannot be related to the recorded seismic activity, we can assume that it represents a non-seismic event.

## ACKNOWLEDGEMENTS

During this work M. Calò was funded by GEISER European Project (FP7: 241321). We thank the GEIE Exploitation Minière de la Chaleur for the hydraulic data. We also thank L. Dorbath for very fruitful and constructive discussions. Finally we very sincerely thank the editor and an anonymous reviewer who helped improve the quality of the manuscript.

## REFERENCES

- Beauce, A., Fabriol, H., Le Masne, D., Cavoit, C., Mechler, C. & Chen, X., 1991. Seismic studies on the HDR site of Soultz-sous-Forêts (Alsace, France), *Geotherm. Sci. Tech.*, **4**, 239–266.
- Calò, M., Dorbath, C., Luzio, D., Rotolo, S.G. & D’Anna, G., 2012. Seismic velocity structures of southern Italy from tomographic imaging of the Ionian slab and petrological inferences, *Geophys. J. Int.*, **191**, 751–764.
- Calò, M., Dorbath, C., Cornet, F.H. & Cuenot, N., 2011. Large-scale aseismic motion identified through 4-D P-wave tomography, *Geophys. J. Int.*, **186**, 1295–1314.
- Calò, M., Dorbath, C., Luzio, D., Rotolo, S.G. & D’Anna, G., 2009. Local Earthquakes Tomography in the southern Tyrrhenian region: geophysical and petrological inferences on subducting lithosphere, in *Subduction Zone Geodynamics, Frontiers in Earth Sciences*, pp. 85–99, eds Lallemand, S. & Funicello, F., Springer-Verlag, Berlin, Heidelberg.
- Calò, M., 2009. Tomography of subduction zones using regional earthquakes: methodological developments and application to the Ionian slab, *PhD thesis*, EOST, University of Strasbourg, <http://tel.archivesouvertes.fr/tel-00438598/en/2>.
- Charl ty, J., 2007. Propri t s physiques du r servoir de Soultz-sous-For ts   partir de l’analyse fine de la sismicit  induite, *PhD thesis*, University of Louis Pasteur, Strasbourg, France.
- Charl ty, J., Cuenot, N., Dorbath, L., Dorbath, C., Haessler, H. & Frogneux, M., 2007. Large earthquakes during hydraulic stimulations at the geothermal site of Soultz-sous-For ts, *Int. J. Rock Mech. Min. Sci.*, **44**, 1091–1105.
- Charl ty, J., Cuenot, N., Dorbath, C. & Dorbath, L., 2006. Tomographic study of the seismic velocity at the Soultz-sous-For ts EGS/HDR site, *Geothermics*, **35**, 532–543.
- Cuenot, N., Dorbath, C. & Dorbath, L., 2008. Analysis of the microseismicity induced by fluid injection in the Hot Dry Rock site of Soultz-sous-For ts (Alsace, France): implications for the characterization of the geothermal reservoir properties, *Pure appl. Geophys.*, **165**, 797–828.
- Cuenot, N., Charl ty, J., Dorbath, L. & Haessler, H., 2006. Faulting mechanisms and stress regime at the European HDR site of Soultz-sous-For ts, France, *Geothermics*, **35**, 561–575.
- Cuenot, N., Charl ty, J., Dorbath, L., Dorbath, C., Frogneux, M., Haessler, H. & Sahr, J., 2005. EOST contribution to the seismological studies at Soultz-sous-For ts for the period 2001–2004, in *Proceedings of the EHDRA Scientific Conference*, Soultz-sous-For ts, France, 17–18 March, p. 9.
- Dezayes, C., Valley, B., Maqua, E., Syren, G. & Genter, A., 2005. Natural fracture system of the Soultz granite based on UBI data in the GPK3 and GPK4 wells, in *Proceedings of the EHDRA Scientific Conference*, Soultz-sous-For ts, France, 17–18 March, p. 9.
- Dezayes, Ch., Genter, A. & Gentier, S., 2004. Fracture network of the EGS geothermal reservoir at Soultz-sous-For ts (Rhine Graben, France), in *Proceedings of the Geothermal Resource Council, Annual Meeting*, Vol. 28, pp. 213–218, Palm Springs, California, USA.
- Dezayes, Ch., Genter, A., Homeier, G., Degouy, M. & Stein, G., 2003. Geological study of GPK-3 HFR borehole (Soultz-sous-For ts, France), Open file Rep. BRGM/RP-52311-FR, 128 pp.
- Dorbath, L., Cuenot, N., Genter, A. & Frogneux, M., 2009. Seismic response of the fractured and faulted granite of Soultz-sous-For ts (France) to 5 km deep massive water injections, *Geophys. J. Int.*, **177**, 653–675.
- Julian, B.R. & Foulger, G.R., 2010. Time-dependent seismic tomography, *Geophys. J. Int.*, **182**, 1327–1338.
- Leonard, M. & Kennett, B.L.N., 1999. Multi-component autoregressive techniques for the analysis of seismograms, *Phys. Earth planet. Inter.*, **113**, 247–263.
- Nami, P., Schellschmidt, R., Schindler, M. & Tischner, T., 2008. Chemical stimulation operations for reservoir development of the deep crystalline HDR/EGS system at Soultz-sous-For ts (France), in *Proceedings of the 33th Workshop on Geothermal Reservoir Engineering*, Stanford University, Stanford, CA, USA.
- Nami, P., Schindler, M., Tischner, T., Jung, R. & Teza, D., 2007. Evaluation of stimulation operations and current status of the deep Soultz wells prior to power production, in *Proceedings of the EHDRA Scientific Conference*, Soultz-sous-For ts, France, 28–29 June, p. 11.
- Schindler, M., Nami, P., Schellschmidt, R., Teza, D. & Tischner, T., 2008. Summary of hydraulic stimulation operations in the 5 km deep crystalline HDR/EGS reservoir at Soultz-sous-For ts, in *Proceedings of the Thirty-Third Workshop on Geothermal Reservoir Engineering*, Stanford University, Stanford, CA, USA, p. 9.
- Schoenball, M., Baujard, C., Kohl, T. & Dorbath, L., 2012. The role of triggering by static stress transfer during geothermal reservoir stimulation, *J. geophys. Res.*, **117**, B09307, doi:10.1029/2012JB009304.
- Toomey, D.R. & Foulger, G.R., 1989. Tomography inversion of local earthquake data from the Hengill Gressdalur central volcano complex, Iceland, *J. geophys. Res.*, **94**(B12), 17 497–17 510.
- Zhang, H. & Thurber, C.H., 2003. Double-difference tomography: the method and its application to the Hayward fault, California Bull, *Seism. Soc. Am.*, **93**, 1175–1189.

## APPENDIX A

To assess the reliability of our results and to show the resolution power of the data and method we build a synthetic model characterized by a low cross-shaped  $P$  velocity anomaly of  $-1.5$  per cent with respect to the initial 1-D velocity distribution (Fig. A1a). The body is placed around the open-hole section of GPK3. Vertical section AB shows the velocity pattern at depth. With the same configuration of earthquakes and stations as in the real inversion, we calculate synthetic traveltimes for Set N 7. This set contains 283 events and represents one of the most representative sets in terms of shape of the seismic cloud. We simulate the possible picking errors by adding a vector of random errors with standard deviation equal to 0.01 s. The 1-D initial model is then used as starting velocity distribution for the inversion of the perturbed synthetic database.

Fig. A1(b) shows the results after the inversion of the synthetic data using only the tomoDD code. The low  $V_P$  anomaly is recovered in the region around the foci and the cross-shaped pattern is roughly recovered. This test highlights the fact that the double difference tomographic method applied to small and very concentrated data sets is able to recover the velocity structures in the regions near the events with satisfactory reliability.

Fig. A1(c) shows the velocity model obtained with the WAM method. We must bear in mind that this model is obtained by the weighted mean of 15 different velocity models previously obtained with tomoDD. Here the cross-shaped anomaly is well recovered also in the border areas. Also, the vertical section shows that the model exhibits no strong artefacts.

With this test we demonstrate that the method used (tomoDD plus WAM) is able to recover the velocity structures in the volume where  $DWS > 10$ .

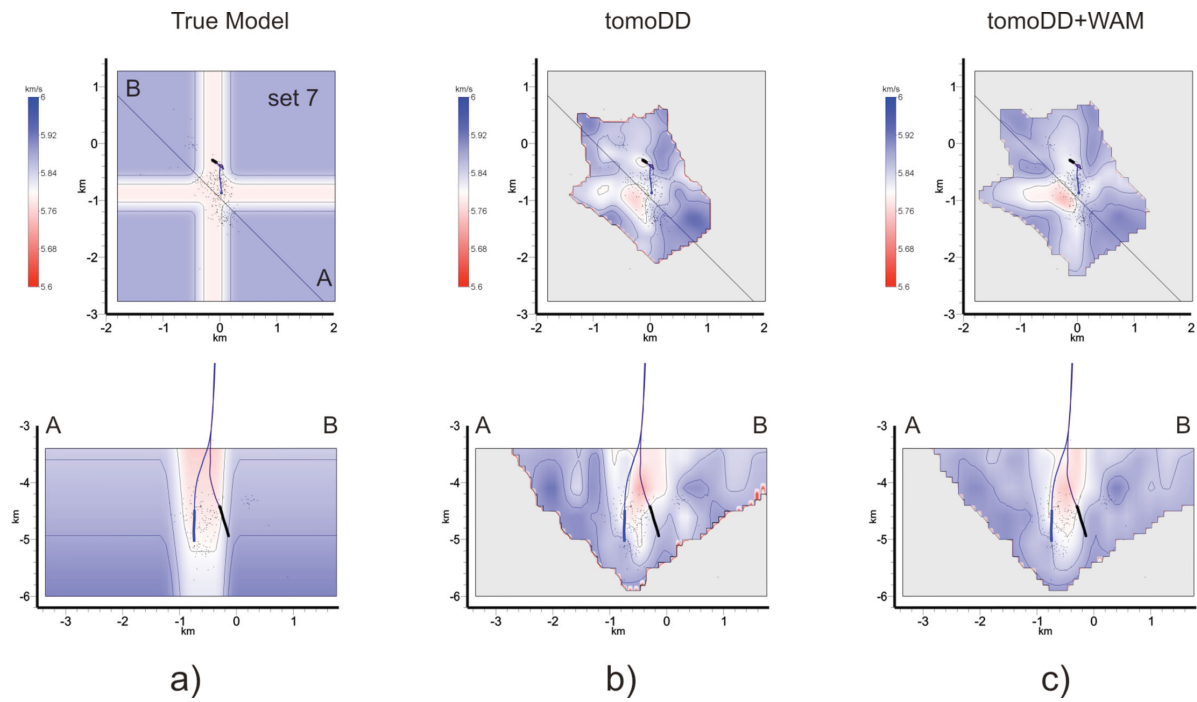


**Figure A1.** (a) Map view at 4.6 km depth and vertical section (AB) of the  $V_p$  model used to calculate the synthetic traveltimes; (b) map view and cross sections of the model obtained with tomoDD only for the Set N 7; (c) model obtained with the tomoDD method added to WAM.

The WAM method allows calculating a Weighted Standard Deviation (WSTD) of the velocity estimates. The WSTD is calculated directly using the velocity distributions used to build the WAM and with the same weighting scheme as to obtain the final velocity. It describes the variability of the models that have been used and

it provides an estimation of the dependence of the single models to the input parameters. Here are reported the horizontal sections at 4.6 km depth (Fig. A2) and the vertical ones (Fig. A3) of the 13 WSTD distributions calculated for the corresponding seismic velocity models.

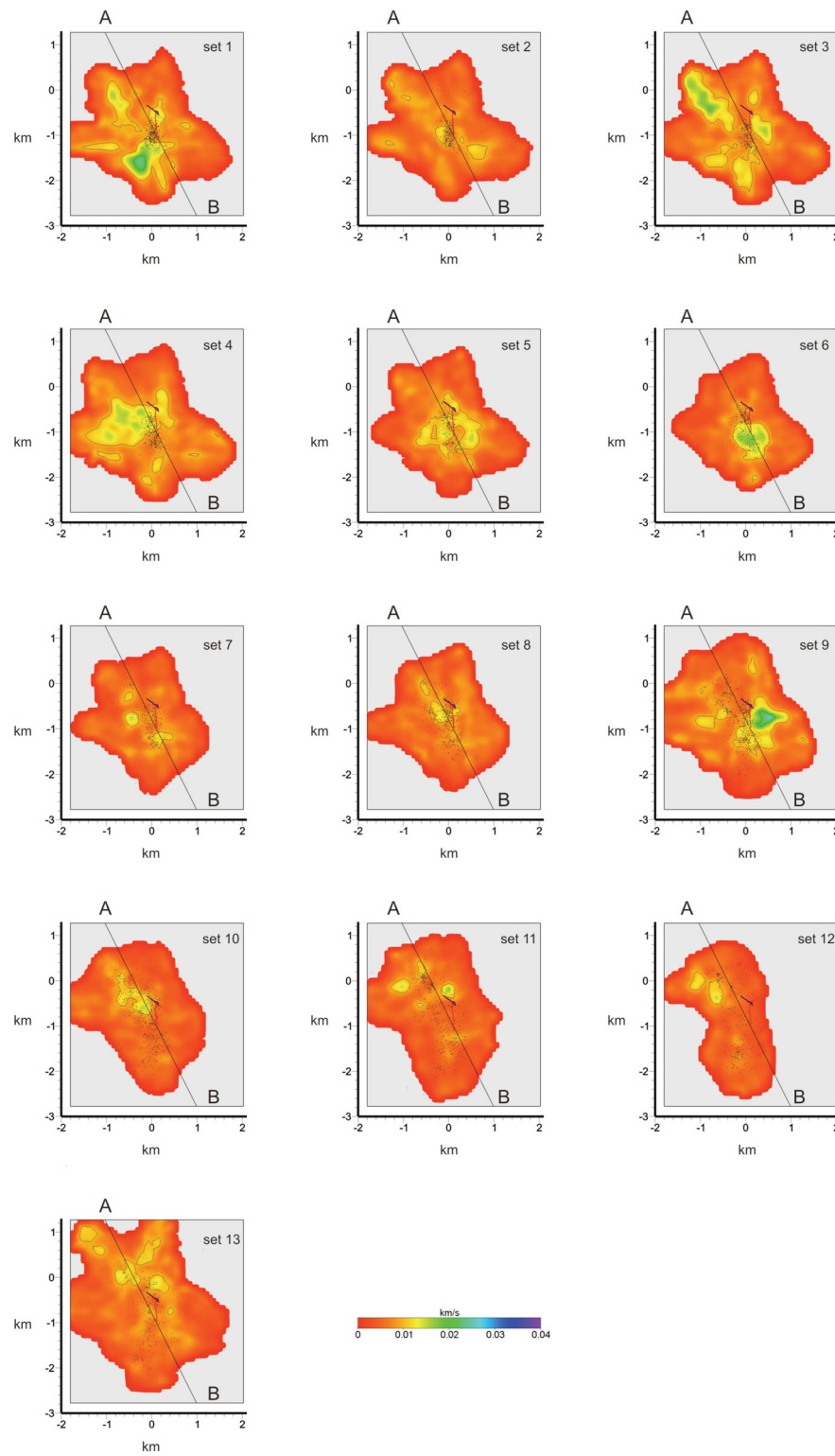
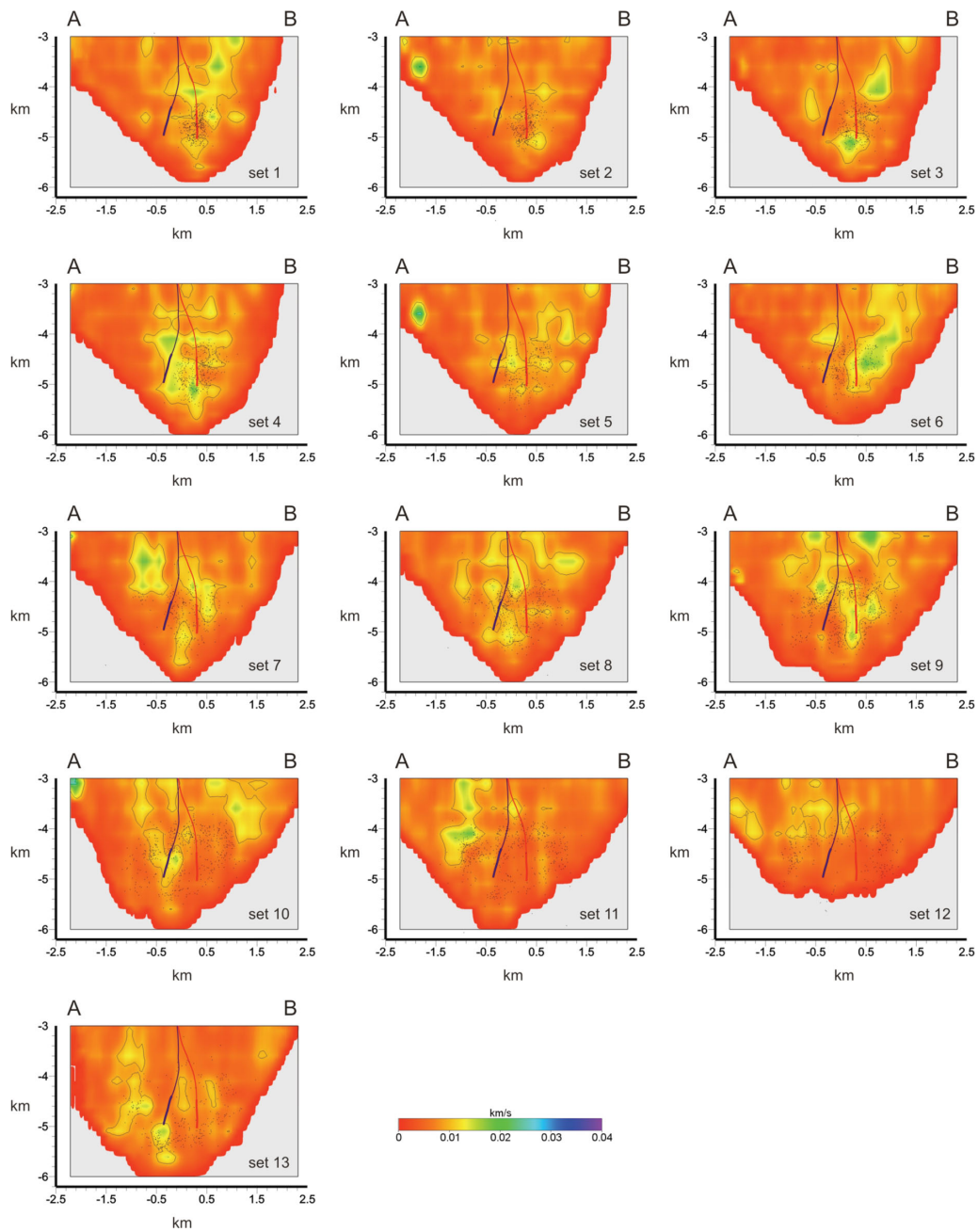


Figure A2. Horizontal slices at 4.6 km of depth of the WSTDs for the 13 tomograms.



**Figure A3.** Vertical sections of the WSTDs for the 13 tomograms.

## APPENDIX B

Evolution of the  $P$ -wave seismic velocity at 4.6 km depth (Fig. B1) and corresponding vertical sections (Fig. B2) during the 2000 stimulation test (after Calò *et al.* 2011). Images are in chronological order from Set 1 to Set 14. The black dots are the projections of the

events used to obtain the  $V_p$  models. Profiles A–B are the traces of the vertical sections.

Fig. B3 reports the evolution of the microseismic cloud. The radius of each circle is proportional to the magnitude and the projection of the injection well is indicated as a black line.

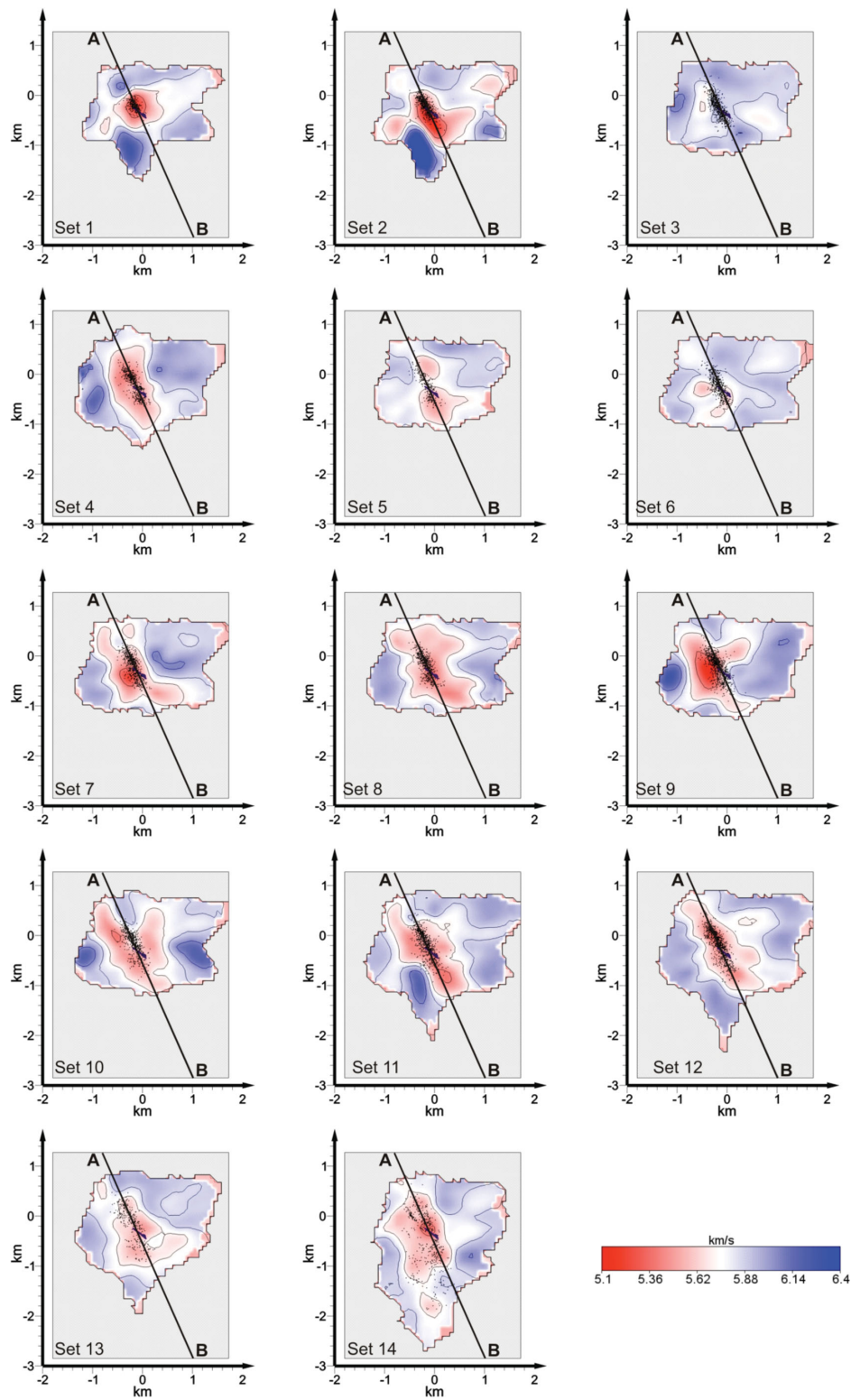
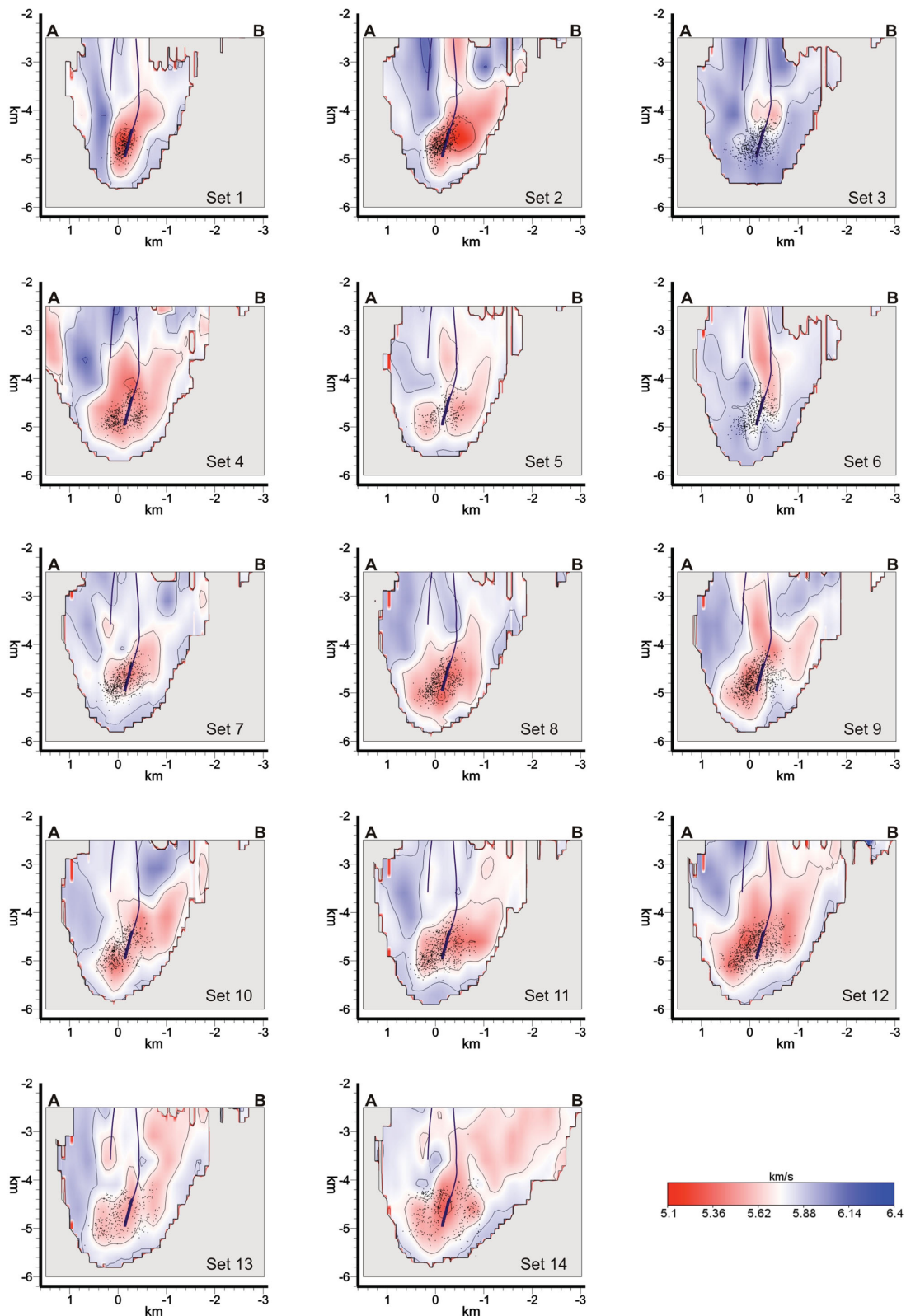


Figure B1. Evolution of the *P*-wave seismic velocity at 4.6 km depth during the 2000 stimulation test (after Calò et al. 2011).



**Figure B2.** Vertical sections of the  $V_p$  models along traces A–B reported in B1 (after Calò et al. 2011).

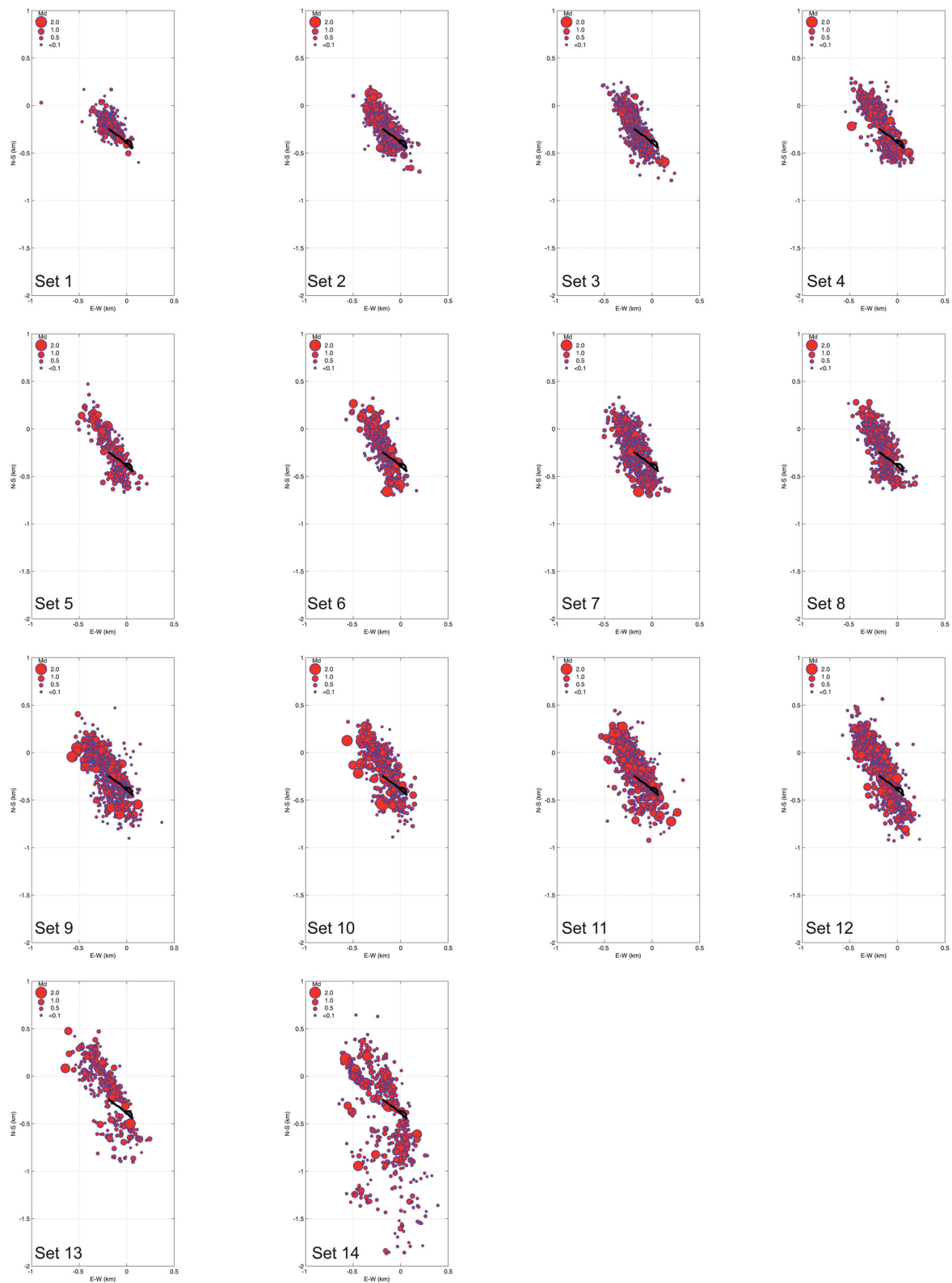


Figure B3. Evolution of the microseismic cloud recorded during the 2000 stimulation test (after Calò et al. 2011).